THE JOURNAL OF PHYSICAL CHEMISTRY Letters

Letter

Cite This: J. Phys. Chem. Lett. 2018, 9, 628–634

pubs.acs.org/JPCL

Electrostatic Estimation of Intercalant Jump-Diffusion Barriers Using Finite-Size Ion Models

Nils E. R. Zimmermann,*[,†] Daniel C. Hannah,[‡] Ziqin Rong,[§] Miao Liu,[‡] Gerbrand Ceder,[‡,⊥] Maciej Haranczyk,[†] and Kristin A. Persson[‡,⊥]

[†]Computational Research Division and [‡]Materials Sciences Division, Lawrence Berkeley National Laboratory, Berkeley, California 94720, United States

[§]Department of Materials Science and Engineering, Massachusetts Institute of Technology, Cambridge, Massachusetts 02139, United States

[⊥]Department of Materials Science and Engineering, University of California, Berkeley, California 94720, United States

Supporting Information

ABSTRACT: We report on a scheme for estimating intercalant jump-diffusion barriers that are typically obtained from demanding density functional theory-nudged elastic band calculations. The key idea is to relax a chain of states in the field of the electrostatic potential that is averaged over a spherical volume using different finite-size ion models. For magnesium migrating in typical intercalation materials such as transition-metal oxides, we find that the optimal model is a relatively large shell. This data-driven result parallels typical assumptions made in models based on Onsager's reaction field theory to quantitatively estimate electrostatic solvent effects. Because of its efficiency, our potential of electrostatics-finite ion size (PfEFIS) barrier estimation scheme will enable rapid identification of materials with good ionic mobility.

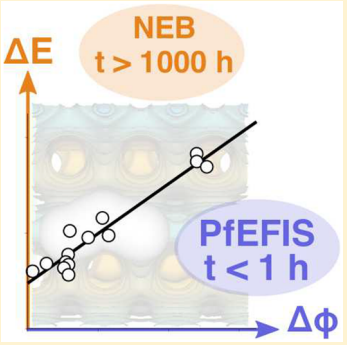

Intercalation is the reversible insertion of a guest species into a solid host structure such that the host maintains its basic structural features.[1−3] The host structure is therefore described as a "breathing matrix",[4] and it can be an insulator, semiconductor, or a metal.[1] Transition metal oxides (TMO) are particularly interesting because they have been extensively studied as cathode candidates for high-energy-density secondary batteries since the 1970s.[1,3,5−7] Lithium has been the dominant intercalation ion,[1] and the efforts have led to the now widespread use of Li-ion technology as rechargeable batteries.[3] TMOs are typically divided into layered and nonlayered materials.[3] In the latter, there usually exists a size limitation for the intercalating atom.[1] Because the magnesium ion has a comparable size to Li^+, Mg^{2+} intercalating into TMOs has been considered since the early 1990s[8] as a promising alternative to Li-ion technology in order to increase energy density, address safety/toxicity concerns, and reduce costs.[9] Hence, magnesium arguably represents the most studied multivalent ion from a guest-species perspective.

A critical aspect of the usability of a certain intercalation system (guest + host) is that the (multivalent) ion transport through the solid host structure be facile.[9,10] Since the transport is governed by jump diffusion,[10,11] it is an activated process[12,13] in which a free energy barrier impedes the migration of an intercalated ion from one site to an adjacent site (Figure 1). Neglecting entropic changes to the free energy along the path, the main physical (energy) barrier contributions should be

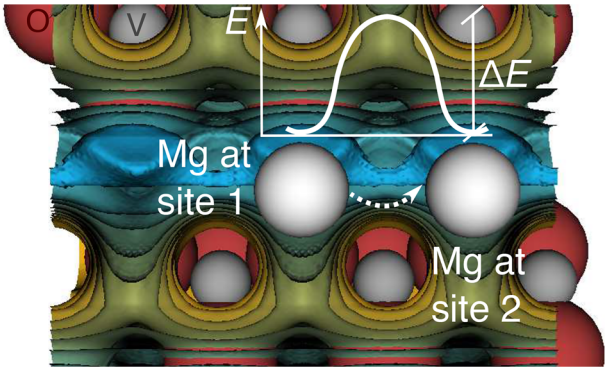

Figure 1. A magnesium ion (large white spheres) intercalated in δ-V_2O_5 (V: gray; O: red) hops from site 1 to site 2 and, thereby, experiences an energy barrier Δ*E*. The change of electrostatic potential (isosurfaces) along the path may be used to estimate Δ*E*.

1. *electrostatic interactions* of the ion within the empty host structure (i.e., based on the electrostatic field in the host structure before inserting the ion);[10]
2. *polarization* at the intercalation site (i.e., electronic relaxation after inserting the ion into the host);[10] and,

Received: December 3, 2017
Accepted: January 10, 2018
Published: January 10, 2018

DOI: 10.1021/acs.jpclett.7b03199
J. Phys. Chem. Lett. 2018, 9, 628–634

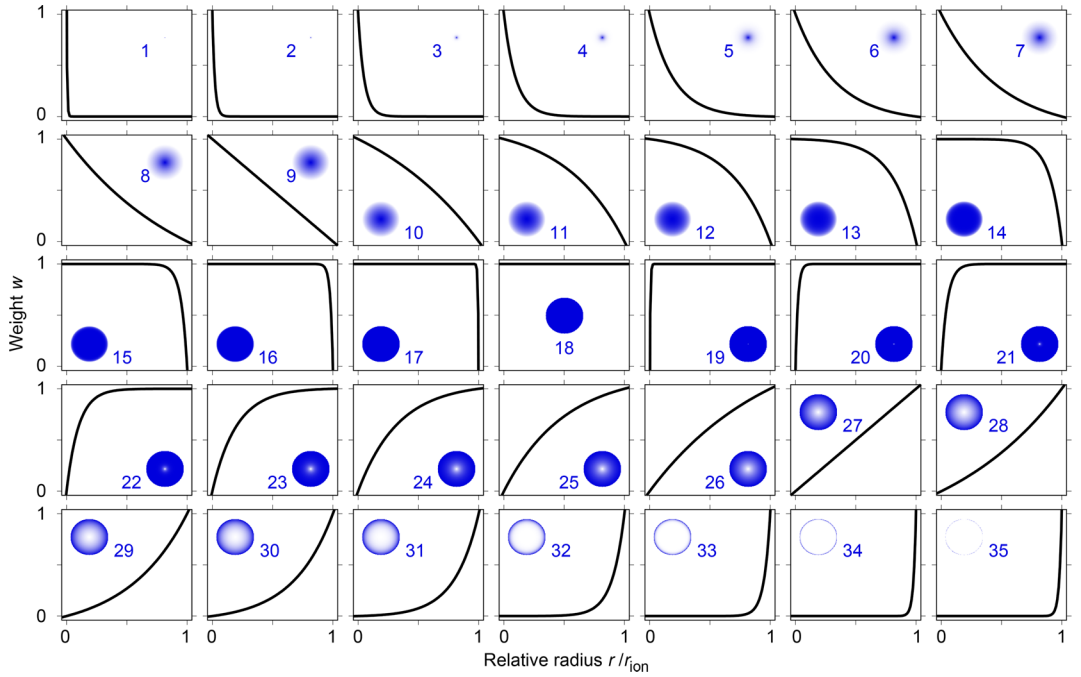

Figure 2. Weight functions, w_i, (black lines) defining the different ion models tested in this work, 2D graphical representations of the models (blue areas), as well as indexes (blue integers) assigned to each ion model.

3. (limited) *elastic contributions*[14] (i.e., ionic relaxation, usually preserving the framework type).

The electrostatic contribution is especially important for two reasons. First, electrostatics are known to be the main force holding an ion in an oxide material at a given site.[13] This enables us to compute a first-order estimate of the intercalation migration barrier on the basis of electrostatics alone. Second, the electrostatic potential can be readily and accurately determined for the considered host systems by electronic density functional theory[15,16] (DFT) calculations, providing a simple route to barrier estimates. As the ion size influences the intercalation behavior, the central question that arises is the following: how do we account for the finite ion size when the electrostatic potential is typically calculated for an infinitesimal small test particle? Here we systematically investigate the possibility to electrostatically estimate Mg migration barriers in typical ionic intercalation hosts (predominantly transition metal oxides). As such barrier estimates are usually derived from computationally intensive DFT-coupled rare events methods, a simple electrostatics-based metric presents an appealing, less computationally demanding alternative. We therefore developed the **P**otential **o**f **E**lectrostatics **F**inite-**I**on **S**ize (PfEFIS) framework, which combines readily computable DFT-derived electrostatic potential data with finite-size ion models and a zero spring-constant living elastic-band algorithm.

The electrostatic work, W_{el}, of bringing a particle of charge q and negligible size from infinity into an electrostatic field φ at position $\mathbf{p}$ is[17]

$$W_{el} = q\varphi(\mathbf{p}) \tag{1}$$

In order to determine the typical work of a finite-size ion on the basis of the electrostatic potential, we have to account for the nonvanishing ion extent. We therefore average the electrostatic potential at a given point $\mathbf{p}$ over a spherical range Ω of radius r_{ion}. Furthermore, we use weighting factors, $w(r)$, for the averaging which depend on the distance $r = \|\mathbf{p} - \tilde{\mathbf{p}}\|$ from $\mathbf{p}$. Different functions for the weighting factors are considered, all of which belong to a family of shifted and scaled exponential functions:

$$w_1(r;\, C,\, r_{ion}) = \frac{\exp(-Cr/r_{ion}) - \exp(-C)}{1 - \exp(-C)} \tag{2}$$

$$w_2(r;\, C,\, r_{ion}) = \frac{1 - \exp(-C(1 - r/r_{ion}))}{1 - \exp(-C)} \tag{3}$$

$$w_3(r;\, C,\, r_{ion}) = \frac{1 - \exp(-Cr/r_{ion})}{1 - \exp(-C)} \tag{4}$$

$$w_4(r;\, C,\, r_{ion}) = \frac{\exp(C(r/r_{ion} - 1)) - \exp(-C)}{1 - \exp(-C)} \tag{5}$$

The ordered set of functions, $\{w_1, w_2, w_3, w_4\}$, represents a change in ion model type via the parameter C from point charge ($\lim_{C\to\infty} w_1(r;\, C,\, r_{ion})$) over full sphere ($\lim_{C\to\infty} w_2(r;\, C,\, r_{ion})$ and $\lim_{C\to\infty} w_3(r;\, C,\, r_{ion})$) to a shell-like model ($\lim_{C\to\infty} w_4(r;\, C,\, r_{ion})$). Using a certain weighting factor function, w_i, the volume-averaged electrostatic potential, $\bar{\varphi}_i$, is given by

$$\bar{\varphi}_i(\mathbf{p}) = \int_\Omega w_i(r;\, C,\, r_{ion})\varphi(\tilde{\mathbf{p}})\mathrm{d}\tilde{\Omega} \Big/ \int_\Omega w_i(r;\, C,\, r_{ion})\,\mathrm{d}\tilde{\Omega} \tag{6}$$

We also use another weighting function, $w_5(r;\, C,\, r_{ion}) = 1$, which represents a homogeneous sphere with respect to computing averages (i.e., $w_5(r;\, C,\, r_{ion}) = \lim_{C\to\infty} w_2(r;\, C,\, r_{ion}) = \lim_{C\to\infty} w_3(r;\, C,\, r_{ion})$).

Figure 2 depicts all 35 ion models considered in our work, and it enumerates the models for plotting purposes below. The weight-function type and parameter C associated with each

DOI: 10.1021/acs.jpclett.7b03199
J. Phys. Chem. Lett. 2018, 9, 628−634

model can be found in the Supporting Information (SI1.2). The first few models resemble point charges, a model type that is commonly used to analyze electrostatics and predict charges by using information from ab initio calculations.[18−21] The models become then progressively more diffusive to turn into a homogenuous spheres (center row). The sphere model might be a natural choice for our purposes because the inserted ion will occupy the entire spherical space. The last models look like hollow shells, which have physical significance because the charge on an ion is typically thought to uniformly distribute on the ion's surface;[17] for this reason, similar models are used in a slightly different context, as described next.

To avoid confusion with mechanistic core−shell models[22] that are used in force fields to mimic polarizability[23,24] note that we refer here to a volumetric shell model. Our shell is the outer region of a sphere that has a (much) higher weight for computing volume averages than the sphere's core region, contrasting force field-related core−shell models in which a massless shell particle is tethered to a heavy core particle via a harmonic spring.[22,23] Our electrostatics-based approach, specifically with the volumetric shell model(s), has, however, similarities with spherical cavity Onsager models[25,26] used in apparent surface charge-dielectric continuum solvation models such as the conductor-like screening model (COSMO).[27] These models are, for example, used to accurately predict partition coefficients of solutes in solvents on the basis of density functional theory calculations.[27−29]

The electrostatic potential within a host material can be readily determined via the Hartree potential, V_H, from DFT calculations with the Vienna Ab initio Simulation Package[30] (VASP) because $V_H(\mathbf{p}) = -\varphi(\mathbf{p})$.[31] We note (i) that the Hartree potential refers here to the potential containing electronic *as well as* ionic contributions, and (ii) that the integrations are in practice performed as discretized sums.

We determine the minimum energy path (MEP) of an input chain of states to our volume-averaged electrostatic-potential field using an elastic band (EB) algorithm.[32] The elastic band contains N_{img} images (or, states), and the target function, $\mathcal{T}$, to be minimized is[33,34]

$$\mathcal{T}(\mathbf{p}_1,...,\mathbf{p}_{N_{img}}) = \sum_{i=2}^{N_{img}-1} \bar{\varphi}(\mathbf{p}_i) + \sum_{i=1}^{N_{img}-1} 0.5k \left|\left|\mathbf{p}_i - \mathbf{p}_{i+1}\right|\right|^2 \quad (7)$$

Our implementation consists of three basic steps. First, the two end points of the band are relaxed without any constraints so that they both move to their respective nearest local minimum. Second, we add more images between any two consecutive points along a straight line such that neighboring images are at most 0.2 Å apart. Finally, we iterate the EB until the magnitude of the total (band) force,

$$f^{tot} = \sum_{i=2}^{N_{img}-1} ||\mathbf{f}_i^{\perp} + \mathbf{f}_i^{spr}|| \quad (8)$$

changes by less than 5%. The force on an individual image is the sum of the spring contribution, $\mathbf{f}_i^{spr} = k((\mathbf{p}_{i+1} - \mathbf{p}_i) - (\mathbf{p}_i - \mathbf{p}_{i-1}))$, and the field contribution ($\mathbf{f}_i = -\nabla\,\bar{\varphi}(\mathbf{p}_i)$); for the latter, we take into account only the part that is orthogonal to the local path ($\mathbf{f}_i^{\perp} = \mathbf{f}_i - (\mathbf{f}_i \cdot \mathbf{t}_i)\,\mathbf{t}_i$, where $\mathbf{t}_i$ is the unit vector pointing from the predecessor image, $i - 1$, to the successor image, $i + 1$; cf., ref 34). Instead of the total force from each individual relaxation step, we use averages calculated over blocks of 10 iteration steps for the convergence criterion. We verify our implementation on a model potential, V_{mod}, with two well-defined stable states (cf., Supporting Information SI1.1). The start and end points of the input paths are perturbed away from the stable states (Figure 3). We observe that the choice of the

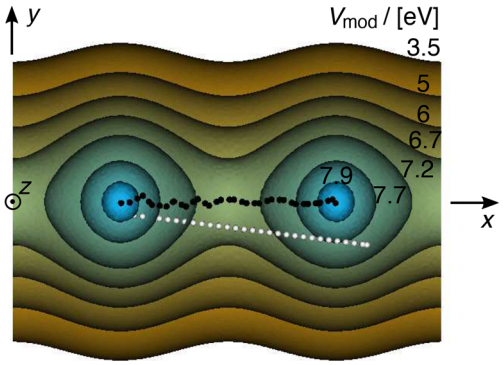

Figure 3. A two-state model potential, V_{mod}, with a barrier of 1 eV was used to validate our elastic band method. The white spheres correspond to an input path, whereas the black spheres display the converged band. For this model potential, we assess the accuracy to be on the order of 99%, by applying the method to 10 distinct input paths for which the end points are subject to different random perturbations away from the stable states.

EB spring constant, k, can lead to the MEP not being traced out accurately. Especially when the spring constant, k, is large, the band gets easily stuck far away from the MEP. We resolve the issue by using a spring constant of zero and adding two algorithmic steps at the end of each EB iteration:

1. Remove an image if it is closer to its predecessor than 0.2 Å.
2. Insert new images so that neighboring images are at most 0.2 Å apart.

The image removal and addition in conjunction with the zero spring constant causes a flow of images from high-energy regions on the MEP of the band toward the end points where they disappear. For this reason, we call it a zero spring constant-living elastic band method. Note that the positions of the images are mapped onto the grid (nearest grid point).

We apply our methodology to Mg migration in 14 TMOs and other typical candidate intercalation compounds for which we have *ab initio* nudged elastic band[35,36] (NEB) barriers available as a benchmark. Using a structure matcher implemented in pymatgen,[37] we identify seven distinct structure groups: layered CoO_2 (1 structure), spinels (4), $CaFe_2O_4$-phase postspinels (2), α-V_2O_5 (1), marokite-phase postspinels (2), β-$VOPO_4$ (1), δ-V_2O_5 (1), and ϵ-$VOPO_4$ (1); more materials information can be found in SI2. The NEB barriers were computed with VASP,[30] and the data can be found in refs 38−42. Apart from the hopping Mg ion, the host structures did not contain any other guest ion. For electrostatic potential calculations, we use the entirely empty relaxed host structure, and we choose DFT settings that are as similar as possible to the NEB calculations. This entails use of the Perdew−Burke−Ernzerhof (PBE) density functionals[43] without +U-correction.[39] Regarding the choice of the density functional, Medvedev et al. have very recently shown that carefully developed conventional general gradient approximation (GGA) functionals can be more accurate in terms of the electron density (and, thus, electrostatic potential) than novel meta-

DOI: 10.1021/acs.jpclett.7b03199
J. Phys. Chem. Lett. 2018, 9, 628−634

GGA and hybrid functionals.[44] Further DFT-related details can be found in the Supporting Information (SI1.3). We use the positions of the hopping ion along a given NEB path as an input chain of configurations to our PfEFIS field-living EB relaxation procedure. An example of the procedure and PfEFIS analysis (Mg in δ-V_2O_5) is given in Figure 4, which underlines

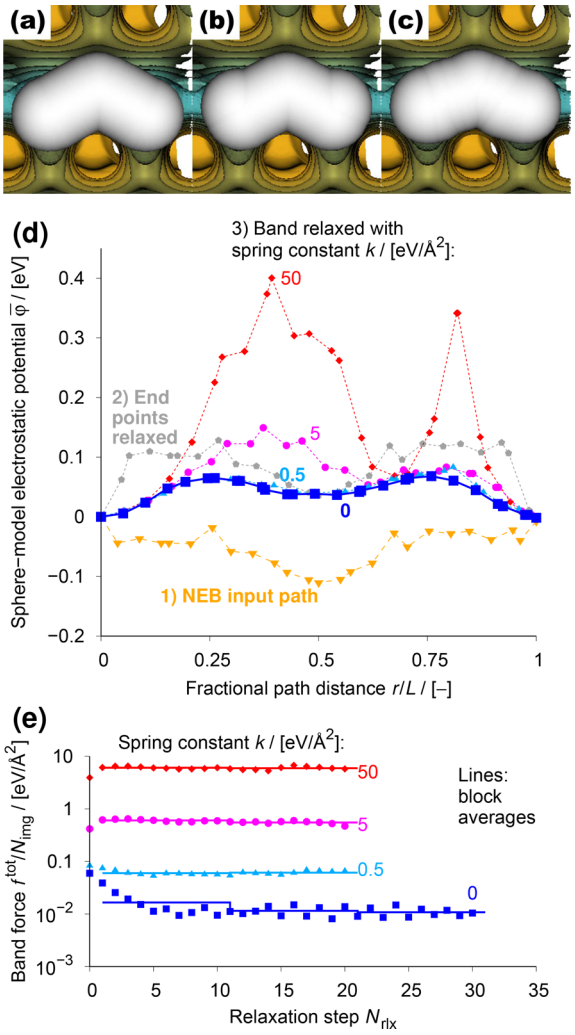

Figure 4. A chain of magnesium atoms (white spheres in a–c) is immersed in the electrostatic field of δ-V_2O_5. The input path (a) is taken from NEB calculations. After an unconstraint relaxation of the end points (b), the remaining band is relaxed with a zero spring constant-living elastic band algorithm until convergence is reached (c). The electrostatic potential profiles, $\bar{\varphi}(r/L)$, using a spherical ion model with r_{ion} = 1.475 Å (d) show that too large a spring constant, k, can give undesirable results (MEP not traced out). (e) Convergence is determined on the basis of the magnitudes of forces on individual images accumulated for the entire band, f^{tot}. If the accumulated force averaged over blocks of 10 relaxation steps (lines) has changed by less than 5%, convergence is reached.

the necessity of a low spring constant. The electrostatic jump-diffusion barrier estimate, ΔE_{el}, is then the product of the maximum electrostatic potential difference, $\Delta\bar{\varphi}$, obtained from the EB relaxation and the charge of the ion (here: q = +2):

$$\Delta E_{el} = q\Delta\bar{\varphi} \tag{9}$$

As mentioned earlier, we investigate 35 different ion models, the definitions of which (i.e., choice of the weight function and parameter C) are provided in the Supporting Information (SI1.2). Ion radii, r_{ion}, are varied between 0.775 and 2.075 Å in steps of Δr_{ion} = 0.05 Å. For each ion model-ion radius pair, we calculate all 14 PfEFIS barrier estimates. Figure 5a displays, for example, the results for a shell ion model of size 1.225 Å. We fit each set of data to a linear function,

$$\Delta E(\Delta E_{el}) = a\Delta E_{el} + b \tag{10}$$

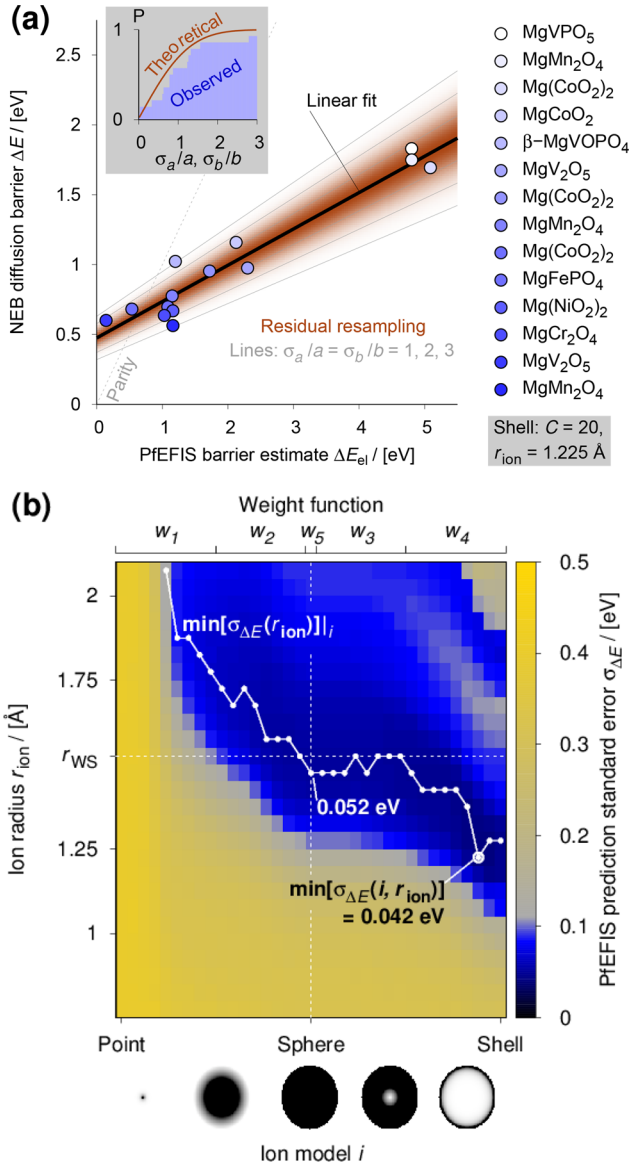

Figure 5. (a) PfEFIS barrier estimate, ΔE_{el}, vs NEB diffusion barrier, ΔE, for a shell-like ion model (C = 20) with size r_{ion} = 1.225 Å. The fitted linear function (black line) can be used to estimate the NEB diffusion barrier. Validation[45] is achieved via residual resampling[46] (brown area and gray solid lines). The inset compares the theoretical and observed accumulative probability, P, that an NEB barrier falls into a prediction range defined by fit parameters a and b and the relative uncertainties σ_a/a and σ_b/b. (b) PfEFIS prediction standard error, $\sigma_{\Delta E}$, as a function of indexed ion model type, i, and ion radius, r_{ion}. Black and yellow indicate negligible and high prediction error, respectively. The optimal ion radius, given a certain ion model, is highlighted by white dots. For comparison, r_{WS} indicates the Wigner–Seitz radius of Mg as used in the VASP[30] calculations. We also highlight the ranges where different weight functions, w_i, are used (top abscissa labels).

DOI: 10.1021/acs.jpclett.7b03199
J. Phys. Chem. Lett. 2018, 9, 628–634

yielding 35 × 27 = 945 individual linear prediction functions, each of which is specific to a given ion model ($N_{\mathrm{ion,mod}}$ = 35) and radius ($N_{\mathrm{ion,rad}}$ = 27). In order to compare the prediction quality of different models, we compute the standard error,

$$\sigma_{\Delta E} = \sqrt{\sum_{i=1}^{N_{\Delta E}} (\Delta E_i - \Delta E(\Delta E_{\mathrm{el},i}))^2 / N_{\Delta E}} \tag{11}$$

between each prediction function (linear fit) and the $N_{\Delta E}$ = 14 actual NEB barriers, ΔE_i. All standard errors are plotted in Figure 5b. The optimal model (i.e., with the smallest error) is shell-like (w_4, C = 20) and of size 1.225 Å ($\sigma_{\Delta E}$ = 0.042 eV). The best strictly spherical model has a slightly higher standard error (0.052 eV) and a radius (1.475 Å) that is comparable to the Wigner−Seitz radius (1.524 Å). The fit parameters, a and b, are 0.26 and 0.475 eV as well as 0.267 and 0.404 eV for the best shell and best sphere model, respectively.

The systematic model comparison is especially intriguing for two reasons. First, the optimal radius of each ion model (white path in Figure 5b) is always much larger than typical Mg^{2+} radii (0.71 Å to 1.03 Å; cf., ref 47) . Therefore, regions far away from the actual ion position seem to be more decisive for the energy profile along the path [and, thus, also for the (reversible) work of ion insertion into an empty host structure] than commonly expected. Second, the prediction error landscape exhibits a peculiar trend. Similarly reliable predictions (similar $\sigma_{\Delta E}$) can be obtained when the ion model changes from a diffusive point over a sphere to a shell, given that the ion radius is successively decreased. Our results suggest therefore that unexpectedly distant but spatially narrow regions around an ion are particularly important for the ion insertion work. This data-driven insight becomes physically meaningful when we compare our approach to reaction field models that have been used successfully in solvation problems for many decades now.[25−29] In both cases, we create a (molecular or ionic) cavity in an electrostatic field, and, subsequently, we use the electrostatic potential (effectively) on the surface of the cavity to realistically estimate the insertion work of a particle (molecule or ion) into the surrounding medium (solvent or intercalation host material). And, in both cases, the optimal cavity size is larger than the typical molecule, atom, or ion size.[27] Note that the reaction field theory-based prediction models are currently actively expanded to heterogeneous environments such as micelles,[27,48] the (solute) surroundings of which are comparable to our intercalation host materials because they are also structured.

Our systematic model-comparison results together with the similarities to the apparent surface charge-dielectric continuum solvation models[27] opens two valuable strategies for estimating ion jump-diffusion barriers with our approach. On the one hand, if there are no NEB barriers at hand for a given ion migrating in a certain class of systems (e.g., transition metal oxides) that would allow optimization of the ion model, especially of the radius, we can recommend to use the full-sphere model with the Wigner−Seitz radius of the intercalating ion. This is because the full-sphere model yields similarly small errors as the optimal (shell) model in our case. On the other hand, if there, in fact, are NEB barriers for a given class of system, we recommend to optimize the model, similar to the fitting that is usually done in the dielectric continuum solvation models, to increase accuracy.

Despite the excellent linear correlation between PfEFIS estimate and NEB barrier, there are several outliers with deviations of up to 0.24 eV. Differing degrees of electronic and ionic relaxation upon ion insertion are two likely error sources to our PfEFIS estimation scheme. However, this could also be utilized in a physically meaningful way because it allows us to quantitatively assess different contributions to an NEB barrier: (1) electrostatics, (2) electronic relaxation (via "selective dynamics" in VASP, for example), and (3) ionic relaxation. The different barrier contributions could be harnessed in the future as descriptors in machine learning approaches that aim to improve our understanding of intercalant diffusion.

Finally, the uncertainty analysis (brown areas and gray lines in Figure 5a) suggests that, with 99% certainty, we can expect:

1. an NEB barrier will be at most 0.64 eV, given that the PfEFIS estimate is around 0.1 eV, and
2. a PfEFIS estimate of 4.2 eV will give at least an NEB barrier of 1 eV.

In summary, we have introduced the potential of electrostatics-finite ion size (PfEFIS) method, which is reliable in providing a first estimate of the magnesium jump-diffusion barrier in intercalation materials. Because PfEFIS has similar well-grounded thermodynamical foundations as reaction field theory-based prediction methods,[25−29] PfEFIS provides theoretically sound electrostatic estimates of the barriers and, thus, can be used to quantitatively assess the influence of electrostatic interactions on the jump-diffusion barrier. Importantly, PfEFIS is computationally faster, typically by a factor of $\approx 10^4$ (SI3), than a full nudged elastic band (NEB) calculation. When PfEFIS is coupled to an effective path finding tool,[42] the PfEFIS framework is therefore ideally suited to efficiently perform high-throughput diffusion-barrier screenings of spherical ions such as Mg, Li, and Na intercalating into transition metal oxides and similar materials.

■ ASSOCIATED CONTENT

Supporting Information

The Supporting Information is available free of charge on the ACS Publications website at DOI: 10.1021/acs.jpclett.7b03199.

Details on models, parameters, and computational details; list of materials; speed-up factor calculation; list of symbols (PDF)

Movie illustrating application of the living-elastic band method on the model potential (MPG)

■ AUTHOR INFORMATION

Corresponding Author

*E-mail: nerz@lbl.gov.

ORCID

Nils E. R. Zimmermann: 0000-0003-1063-5926

Miao Liu: 0000-0002-1843-9519

Maciej Haranczyk: 0000-0001-7146-9568

Notes

The authors declare no competing financial interest.

■ ACKNOWLEDGMENTS

This work was intellectually led by the U.S. Department of Energy (DOE) Basic Energy Sciences (BES) program—the Materials Project—under Grant No. EDCBEE. We thank Pieremanuele Canepa and Sai Gautam for valuable discussions. Z.R., M.L., and D.H. contributed NEB migration energies as well as local potential calculations and they were supported as part of the Joint Center for Energy Storage Research (JCESR),

DOI: 10.1021/acs.jpclett.7b03199
J. Phys. Chem. Lett. 2018, 9, 628−634

an Energy Innovation Hub funded by the U.S. Department of Energy, Office of Science, and Basic Energy Sciences, subcontract 3F-31144. This research used resources of the National Energy Research Scientific Computing Center, which is supported by the Office of Science of the U.S. Department of Energy under Contract No. DEAC02-05CH11231. Furthermore, this research used resources of the Argonne Leadership Computing Facility, which is a DOE Office of Science User Facility supported under Contract DE-AC02-06CH11357. Lawrence Berkeley National Laboratory is funded by the DOE under award DE-AC02-05CH11231.

REFERENCES

(1) Whittingham, M. S.; Jacobson, A. J. *Intercalation Chemistry*; Academic Press, Inc.: New York, 1982.
(2) Goodenough, J. B.; Park, K.-S. The Li-ion rechargeable battery: a perspective. *J. Am. Chem. Soc.* **2013**, *135*, 1167−1176.
(3) Nitta, N.; Wu, F.; Lee, J. T.; Yushin, G. Li-ion battery materials: present and future. *Mater. Today* **2015**, *18*, 252−264.
(4) Besenhard, J. O.; Eichinger, G. High energy density lithium cells: Part I. Electrolytes and anodes. *J. Electroanal. Chem. Interfacial Electrochem.* **1976**, *68*, 1−18.
(5) Eichinger, G.; Besenhard, J. O. High energy density lithium cells: Part II. Cathodes and complete cells. *J. Electroanal. Chem. Interfacial Electrochem.* **1976**, *72*, 1−31.
(6) Mizushima, K.; Jones, P. C.; Wiseman, P. J.; Goodenough, J. B. Li_xCoO_2 ($0 < x \leq 1$): a new cathode material for batteries of high energy density. *Mater. Res. Bull.* **1980**, *15*, 783−789.
(7) Fergus, J. W. Recent developments in cathode materials for lithium ion batteries. *J. Power Sources* **2010**, *195*, 939−954.
(8) Bruce, P. G.; Krok, F.; Nowinski, J.; Gibson, V. C.; Tavakkoli, K. Chemical intercalation of magnesium into solid hosts. *J. Mater. Chem.* **1991**, *1*, 705−706.
(9) Palacín, M. R. Recent advances in rechargeable battery materials: a chemist's perspective. *Chem. Soc. Rev.* **2009**, *38*, 2565−2575.
(10) Levi, E.; Levi, M. D.; Chasid, O.; Aurbach, D. A review on the problems of the solid state ions diffusion in cathodes for rechargeable Mg batteries. *J. Electroceram.* **2009**, *22*, 13−19.
(11) Singwi, K. S.; Sjölander, A. Resonance absorption of nuclear gamma rays and the dynamics of atomic motions. *Phys. Rev.* **1960**, *120*, 1093−1102.
(12) Eyring, H. The activated complex in chemical reactions. *J. Chem. Phys.* **1935**, *3*, 107−115.
(13) Dowty, E. Crystal-chemical factors affecting the mobility of ions in minerals. *Adv. Mater.* **1980**, *65*, 174−182.
(14) Safran, S. A.; Hamann, D. R. Electrostatic interactions and staging in graphite intercalation compounds. *Phys. Rev. B: Condens. Matter Mater. Phys.* **1980**, *22*, 606−612.
(15) Hohenberg, P.; Kohn, W. Inhomogeneous electron gas. *Phys. Rev.* **1964**, *136*, B864−B871.
(16) Kohn, W.; Sham, L. J. Self-consistent equations including exchange and correlation effects. *Phys. Rev.* **1965**, *140*, A1133−A1138.
(17) Dill, K. A.; Bromberg, S. *Molecular Driving Forces: Statistical Thermodynamics in Biology, Chemistry, Physics, and Nanoscience*, 2nd ed.; Garland Science: Abingdon, U.K., 2011.
(18) Kramer, G. J.; Farragher, N. P.; van Beest, B. W. H.; van Santen, R. A. Interatomic force fields for silicas, aluminophosphates, and zeolites: derivation based on *ab initio* calculations. *Phys. Rev. B: Condens. Matter Mater. Phys.* **1991**, *43*, 5068−5080.
(19) Brand, H. V.; Curtiss, L. A.; Iton, L. E. *Ab initio* molecular orbital cluster studies of the zeolite ZSM-5. 1. Proton affinities. *J. Phys. Chem.* **1993**, *97*, 12773−12782.
(20) Hill, J.-R.; Sauer, J. Molecular mechanics potential for silica and zeolite catalysts based on ab initio calculations. 1. Dense and microporous silica. *J. Phys. Chem.* **1994**, *98*, 1238−1244.
(21) Henkelman, G.; Arnaldsson, A.; Jónsson, H. A fast and robust algorithm for Bader decomposition of charge density. *Comput. Mater. Sci.* **2006**, *36*, 354−360.
(22) Dick, B. G.; Overhauser, A. W. Theory of the dielectric constants of alkali halide crystals. *Phys. Rev.* **1958**, *112*, 90−103.
(23) Sauer, J.; Sierka, M. Combining quantum mechanics and interatomic potential functions in ab initio studies of extended systems. *J. Comput. Chem.* **2000**, *21*, 1470−1493.
(24) Finnis, M. *Interatomic forces in condensed matter*; Oxford University Press: Oxford, U.K., 2003.
(25) Onsager, L. Electric moments of molecules in liquids. *J. Am. Chem. Soc.* **1936**, *58*, 1486−1493.
(26) Karelson, M. M.; Katritzky, A. R.; Szafran, M.; Zerner, M. C. Quantitative predictions of tautomeric equilibria for 2-, 3-, and 4-substituted pyridines in both the gas-phase and aqueous-solutions: combination of AM1 with reaction field-theory. *J. Org. Chem.* **1989**, *54*, 6030−6034.
(27) Klamt, A. The COSMO and COSMO-RS solvation models. *WIRes: Comput. Mol. Sci.* **2011**, *1*, 699−709.
(28) Miertuš, S.; Scrocco, E.; Tomasi, J. Electrostatic interaction of a solute with a continuum. A direct utilization of ab initio molecular potentials for the prevision of solvent effects. *Chem. Phys.* **1981**, *55*, 117−129.
(29) Tomasi, J.; Mennucci, B.; Cammi, R. Quantum mechanical continuum solvation models. *Chem. Rev.* **2005**, *105*, 2999−3093.
(30) Kresse, G.; Hafner, J. *Ab initio* molecular dynamics for liquid metals. *Phys. Rev. B: Condens. Matter Mater. Phys.* **1993**, *47*, 558−561.
(31) Giustino, F. *Materials Modelling using Density Functional Theory−Properties and Predictions*; Oxford University Press: New York, 2014.
(32) Peyrard, M.; Aubry, S. Critical behavior at the transition by breaking of analyticity in the discrete Frenkel-Kontorova model. *J. Phys. C: Solid State Phys.* **1983**, *16*, 1593−1608.
(33) Jensen, F. *Introduction to Computational Chemistry*, 2nd ed.; John Wiley & Sons Ltd: West Sussex, England, U.K., 2007.
(34) Sholl, D. S.; Steckel, J. A. *Density Functional Theory−A Practical Introduction*; John Wiley & Sons, Inc.: Hoboken, NJ, 2009.
(35) Mills, G.; Jónsson, H.; Schenter, G. K. Reversible work transition state theory: application to dissociative adsorption of hydrogen. *Surf. Sci.* **1995**, *324*, 305−337.
(36) Henkelman, G.; Uberuaga, B. P.; Jónsson, H. A climbing image nudged elastic band method for finding saddle points and minimum energy paths. *J. Chem. Phys.* **2000**, *113*, 9901−9904.
(37) Ong, S. P.; Richards, W. D.; Jain, A.; Hautier, G.; Kocher, M.; Cholia, S.; Gunter, D.; Chevrier, V. L.; Persson, K. A.; Ceder, G. Python Materials Genomics (pymatgen): A robust, open-source python library for materials analysis. *Comput. Mater. Sci.* **2013**, *68*, 314−319.
(38) Ling, C.; Mizuno, F. Phase stability of post-spinel compound AMn_2O_4 (A = Li, Na, or Mg) and its application as a rechargeable battery cathode. *Chem. Mater.* **2013**, *25*, 3062−3071.
(39) Liu, M.; Rong, Z.; Malik, R.; Canepa, P.; Jain, A.; Ceder, G.; Persson, K. A. Spinel compounds as multivalent battery cathodes: a systematic evaluation based on ab initio calculations. *Energy Environ. Sci.* **2015**, *8*, 964−974.
(40) Rong, Z.; Malik, R.; Canepa, P.; Gautam, G. S.; Liu, M.; Jain, A.; Persson, K.; Ceder, G. Materials design rules for multivalent ion mobility in intercalation structures. *Chem. Mater.* **2015**, *27*, 6016−6021.
(41) Gautam, G. S.; Canepa, P.; Malik, R.; Liu, M.; Persson, K.; Ceder, G. First-principles evaluation of multi-valent cation insertion into orthorhombic V_2O_5. *Chem. Commun.* **2015**, *51*, 13619−13622.
(42) Rong, Z.; Kitchaev, D.; Canepa, P.; Huang, W.; Ceder, G. An efficient algorithm for finding the minimum energy path for cation migration in ionic materials. *J. Chem. Phys.* **2016**, *145*, 074112.
(43) Perdew, J. P.; Burke, K.; Ernzerhof, M. Generalized gradient approximation made simple. *Phys. Rev. Lett.* **1996**, *77*, 3865−3868.
(44) Medvedev, M. G.; Bushmarinov, I. S.; Sun, J.; Perdew, J. P.; Lyssenko, K. A. Density functional theory is straying from the path toward the exact functional. *Science* **2017**, *355*, 49−52.
(45) Tropsha, A.; Gramatica, P.; Gombar, V. K. The importance of being earnest: Validation is the absolute essential for successful

DOI: 10.1021/acs.jpclett.7b03199
J. Phys. Chem. Lett. 2018, 9, 628−634

application and interpretation of QSPR models. *QSAR Comb. Sci.* **2003**, *22*, 69−77.
(46) Good, P. I. *Resampling Methods*, 2nd ed.; Birkhauser: Basel, Switzerland, 2001.
(47) Shannon, R. D. Revised effective ionic radii and systematic studies of interatomic distances in halides and chalcogenides. *Acta Crystallogr., Sect. A: Cryst. Phys., Diffr., Theor. Gen. Crystallogr.* **1976**, *32*, 751−767.
(48) Yordanova, D.; Ritter, E.; Gerlach, T.; Jensen, J. H.; Smirnova, I.; Jakobtorweihen, S. Solute partitioning in micelles: combining molecular dynamics simulations, COSMOmic, and experiments. *J. Phys. Chem. B* **2017**, *121*, 5794−5809.

DOI: 10.1021/acs.jpclett.7b03199
J. Phys. Chem. Lett. 2018, 9, 628−634